

First-principles studies on anomalous electron and spin transport properties in non-trivial spin textures

Fumiyuki ISHII

Nanomaterials Research Institute

Kanazawa University, Kakuma-machi, Kanazawa, Ishikawa 920-1192

1 Abstract

Electron spins can act as inter-converter of electricity, light, sound vibration, and heat [1]. Spin-related transport properties of materials originate in its spin structures of real and momentum space. To design spin conversion materials, we have studied anomalous Nernst effect, i.e., anomalous Hall effect induced by temperature gradient in magnetic materials [2], and Rashba effect [3] and persistent spin helix state [4] in non-magnetic materials.

We have studied the systems with special spin structures applicable to spintronics or thermoelectric conversion based on first-principles density functional calculations using OpenMX [5]. We focused on surfaces, interfaces and 2D system with peculiar spin textures such as Rashba spin textures that can lead to spin-to-charge conversion (from a spin current to a charge current), and skyrmion that can enhances Berry curvatures in momentum space.

2 First-principles methods

We have performed first-principles electronic-structure simulations based on the non-collinear density functional theory (DFT) with two-component spinor wave functions for Kohn–Sham–Bloch orbitals [8,9] using the OpenMX

code [5]. We used the generalized gradient approximation with the Perdew-Burke-Ernzerhof functional to treat the exchange-correlation potential [10]. We used the fully-relativistic total angular momentum dependent norm-conserving pseudopotentials considering the spin–orbit interaction [11,12]. We extended the wave functions using a linear combination of multiple pseudoatomic orbitals [13,14].

To study anomalous Nernst effect, the Wannier90 code was used to construct maximally localized Wannier functions (MLWFs) based on the results of the DFT calculations [15]. We also simulated the transport properties based on the MLWFs using the semiclassical Boltzmann transport theory [16]. We have previously used this method successfully to study the thermoelectric properties of half-Heusler compounds with the formula CoMSb (M=Sc, Ti, V, Cr, and Mn) [17].

In the study of Rashba effect, we deduce the spin polarization in the momentum space from the momentum \mathbf{k} -dependent spin density matrix. The spin density matrices $P_{\sigma,\sigma'}^n(\mathbf{k}) = \int \psi_{\sigma}^{*n}(\mathbf{k}, \mathbf{r}) \psi_{\sigma'}^n(\mathbf{k}, \mathbf{r}) d\mathbf{r}$ are calculated using the spinor Bloch wavefunction, the component of

which is given by $\psi_\sigma^n(\mathbf{k}, \mathbf{r})$ which is obtained from the OpenMX calculations, where σ is the spin index (\uparrow or \downarrow) and n is the band index.

3 Anomalous Nernst effect

We are interested in how to achieve much higher thermoelectric conversion efficiency by effectively manipulating electron-spin degree of freedom. As one possibility, we have been studying Berry-phase-mediated thermoelectric effects, namely the contribution of the anomalous Hall conductivity (AHC) to thermoelectric power. What we target here is the

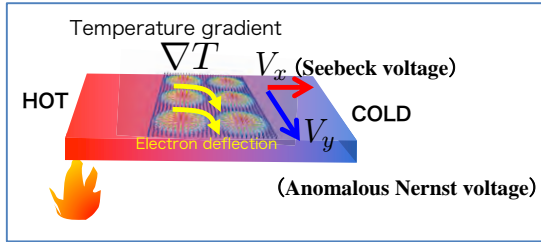


Fig. 1: Thermoelectric effect in skyrmion crystal.

anomalous Nernst effect (ANE), which is a heat-to-electricity conversion observed in magnetic materials and directly related to AHC. We discussed AHC mainly driven by an effective magnetic field, Berry curvature, induced by spin-orbit coupling and/or spin chirality.

We have so far found from computations on simple models that, in the so-called 2D Skyrmion crystal (SkX) phase, where skyrmions are crystallized in two dimensions, the crystal-momentum component of effective magnetic field gives rise to the band structure that could generate large ANE when chemical potential μ

is properly tuned [6]. Fig.1 shows schematic view of thermoelectric effect (Seebeck effect and anomalous Nernst effect) in SkX. Although

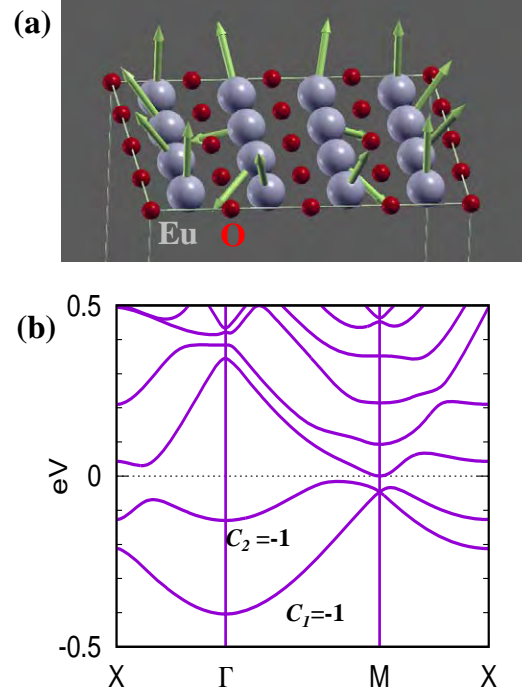


Fig. 2. (a) Calculated spin structures for skyrmion of EuO monolayer model. (b) Calculated band structure and corresponding band-by-band decomposition of Chern number.

the large ANE was most clearly confirmed in the simplest model of square SkX with single s -orbital per site, our subsequent computations on more realistic multi-orbital models of also showed possible large ANE [7].

We have performed first-principles calculations for 2D SkX of EuO monolayer (Fig. 2(a)). The charge density cutoff energy was set at 250 Rydbergs and a regular k -point mesh (20,20,1) was used for the self-consistent calculations (SCFs). A sizable transverse thermoelectric coefficient is predicted to arise in

a SkX assumed on EuO monolayer where carrier electrons are introduced upon a quantum anomalous Hall insulating phase of Chern number $C_{\text{total}} = 2$. This encourages future experiments to pursue such an effect.

To achieve band-by-band analysis for AHC, we have implemented the methods in OpenMX computing Berry curvature on discretized Brillouin zone [18]. The Chern number of each band C_n (n : band index) can be calculated by integrating the Berry curvature.

Figure 2 (b) shows the band structure of electron-doped EuO monolayer. There is a narrow band gap of about 20 meV between the valence band top and conduction band bottom. The occupied two bands with Chern number $C_{\text{total}}=2$ are mainly composed of Eu 5d and 6s characters. We have calculated anomalous Nernst coefficients N by using semiclassical Boltzmann transport theory with constant relaxation time, $\tau = 10$ fs. The Nernst coefficients are related to the conductivity tensor, and these relationships can be represented as shown below [7]:

$$N = \frac{N_0 - \theta_H S_0}{1 + \theta_H^2}$$

where $N_0 = \alpha_{xy}/\sigma_{xx}$, $S_0 = \alpha_{xx}/\sigma_{xx}$, $\theta_H = \sigma_{xy}/\sigma_{xx}$ are the pure Nernst coefficient, pure Seebeck coefficient, and Hall angle ratio, respectively. The electrical conductivity tensors were computed from

$$\sigma_{xx} = \int e^2 \tau \sum_n v_{x,n}^2(k) \left(-\frac{\partial f(\varepsilon_{n,k})}{\partial \varepsilon_k} \right) dk$$

while the AHCs were computed from

$$\sigma_{xy} = e^2 \sum_n \Omega_n^z(k) f(\varepsilon_{n,k}) dk.$$

The thermoelectric conductivity tensors were computed by

$$\alpha_{ij} = \frac{k_B}{e} \int \sigma_{ij}(\varepsilon) \frac{\varepsilon - \mu}{T} \left(-\frac{\partial f(\varepsilon_{n,k})}{\partial \varepsilon_k} \right) d\varepsilon$$

where e , τ , $v_{x,n}^2(k)$, f , $\varepsilon_{n,k}$, \hbar , $\Omega_n^z(k)$, T , k_B and μ are the elementary charge, relaxation time, group velocity of electrons, Fermi-Dirac distribution function, energy, reduced Planck constant, Berry curvature, temperature, Boltzmann's constant, and chemical potential, respectively.

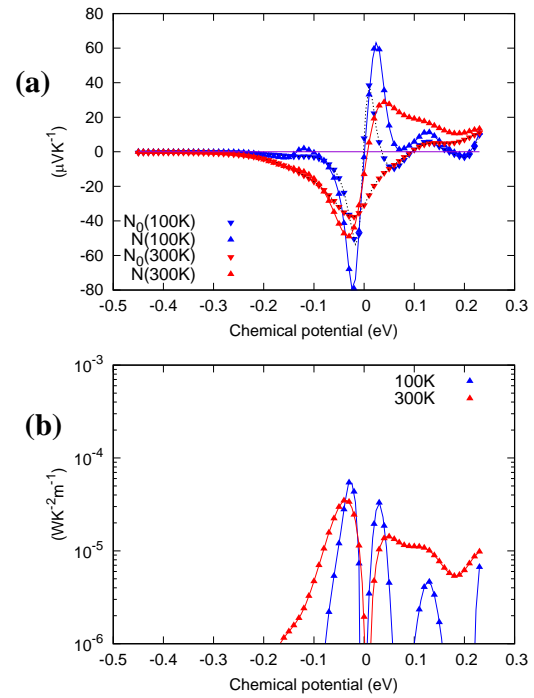


Fig. 3. (a) The chemical potential dependence of anomalous Nernst coefficients and (b) power factors. Results are shown for different values of temperature 100K and 300K. We assumed the constant relaxation time $\tau = 10$ fs.

The calculated chemical potential dependence of Nernst coefficients N , pure Nernst coefficients

and power factor are plotted in Fig 3(a) and (b). The large anomalous Nernst coefficients up to $60 \mu\text{V}/\text{K}$ and power factor up to $70 \mu\text{W}/\text{mK}^2$ can be obtained. Such N arises from the coexistence of large longitudinal thermoelectric coefficient and large Hall angle ratio, realized in the vicinity of a narrow band gap with Chern number $C_{\text{total}} = 2$. The origin of reported other materials are mainly pure Nernst effect, N_0 , in metallic magnetic materials. This is the reason why the anomalous Nernst effect is smaller than Seebeck effect in general. In contrast, electron-doped EuO monolayer is narrow-gap Chern insulator. It is similar to the case that the narrow gap semiconductor shows large Seebeck effects. This demonstrates a prototype of novel class of new thermoelectric materials utilizing the nanoscale topological spin textures, motivating further studies including relevant experiments. We concluded that the SkX and narrow-gap Chern insulators could be candidate materials for thermoelectric applications.

4 Spin-to-charge conversion

In recent years, a phenomenon called spin-to-charge current (SCC) conversion that converts a spin current into a charge current is attracting much attentions [19]. There is inverse Rashba Edelstein effect (IREE) as a more efficient method than inverse spin Hall effect [20] which is one of the origins of the SCC conversion. The SCC conversion by IREE has been reported to occur at the materials interfaces with Rashba

effect. The Rashba effect is an effect of resolving the spin degeneracy in a non-magnetic material whose space inversion symmetry is broken [3]. The efficiency of SCC using IREE is evaluated by the conversion factor λ_{IREE} , i.e., the ratio of the injected (resulted) spin (charge) current J_S (J_C) densities as $\lambda_{\text{IREE}} = J_C/J_S$. The λ_{IREE} is proportional to the Rashba coefficient α_R as $\lambda_{\text{IREE}} = \alpha_R \tau_S/\hbar$ where τ_S is the spin relaxation time and \hbar is reduced planck constant [19].

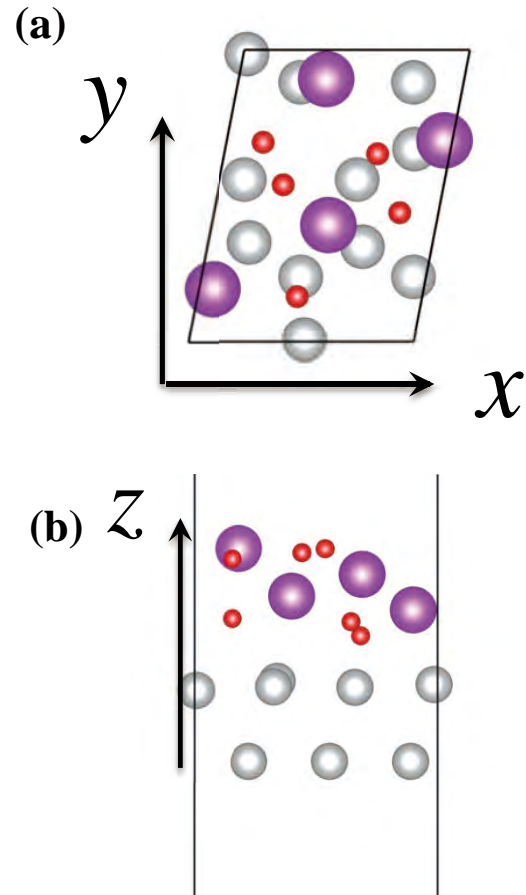


Fig. 4. Calculated model of interfaces noble metal/ α - Bi_2O_3 ; (a) Top view; (b) side view. White, purple and red circles correspond to noble metal, Bismuth and Oxygen.

In order to improve the SCC conversion efficiency, many materials interfaces were

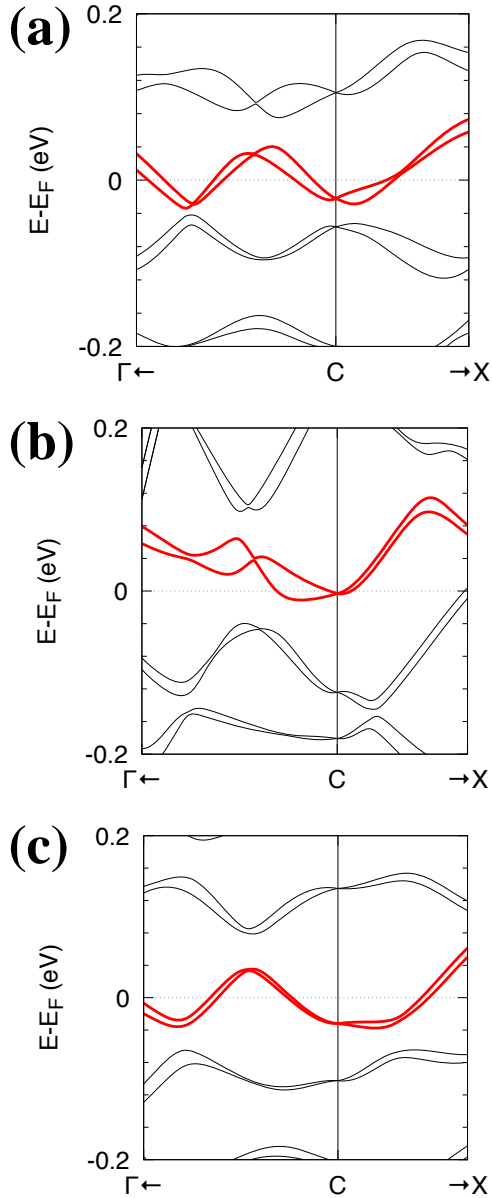


Fig. 5. Band structures for $M(111)/\alpha\text{-Bi}_2\text{O}_3$. (a) $M = \text{Cu}$; (b) $M = \text{Ag}$; (c) $M = \text{Au}$. The enlarged views of the band structures around C-point are shown through each path from C-point to the point dividing $\text{C}\Gamma$ or CX line internally in the ratio 1:4.

studied such as substances with large Rashba coefficients and long spin relaxation time.

Figure 4 shows the interface model of (111) face-centered-cubic noble metal with oxide insulator α -type structure Bi_2O_3 , $M(111)$ ($M = \text{Cu}, \text{Ag}, \text{Au}$)/ $\alpha\text{-Bi}_2\text{O}_3$. Fig. 5(a)-(c) shows the band structure for the $\text{NM}(111)/\alpha\text{-Bi}_2\text{O}_3$ systems, where the symmetry points ($\Gamma, \text{C}, \text{X}$) are those in the first Brillouin zone shown in Fig. 7(a). There is a free-electron-like band around C-point near the Fermi energy for each system, and its Rashba spin splitting is anisotropic.

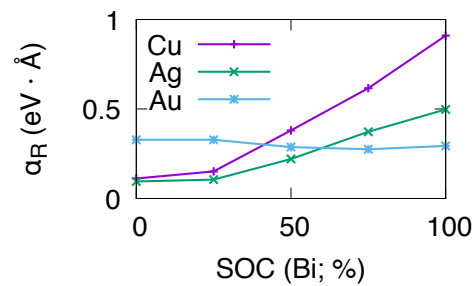


Fig. 6. Strength dependence of spin-orbit coupling (SOC) of Bi on Rashba coefficient for noble metal/ $\alpha\text{-Bi}_2\text{O}_3$.

A trend in the Rashba spin splitting is corresponding to obtained the Rashba coefficients α_R as the average of the ones along $\text{C}\Gamma$ and CX line around C-point. Our calculated α_R are 0.91, 0.50 and 0.29 for $M = \text{Cu}, \text{Ag}$ and Au , respectively, in units of $\text{eV}\cdot\text{\AA}$. The strength dependence of SOC in Bi on the α_R is shown in Fig. 6. For $M = \text{Cu}$ and Ag , the α_R increases as the strength of SOC of Bi increases. When the SOC of Bi is turned off, the α_R becomes zero and this indicates that the SOC of Bi is essential for occurring large α_R . On the other hand, for M

= Au, α_R decreases as the strength of SOC of Bi

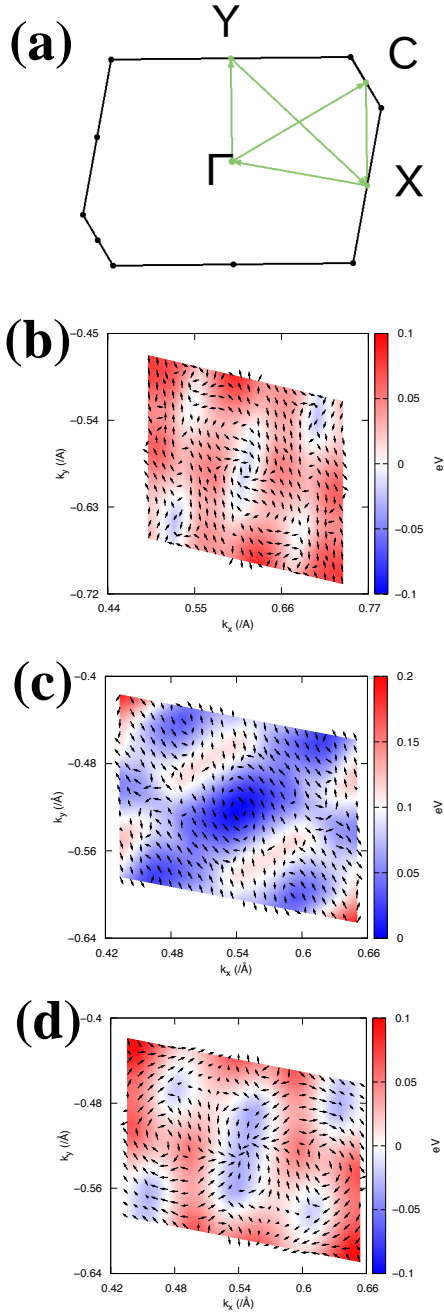


Fig. 7. (a) Schematic of the first Brillouin zone with high symmetry points. Energy dependence of spin textures of lower energy bands in fig. 5 around C point for (b) Cu(111)/ α -Bi₂O₃; (c) Ag(111)/ α -Bi₂O₃; (d) Au(111)/ α -Bi₂O₃.

increases. Even if there is no SOC of Bi, α_R is not zero and this may be originated from the SOC of Au. In the case of $M = \text{Cu}$ and Ag, α_R is more drastically changed compared to Au case. It suggests that the influence on the α_R due to noble metal is different depending on the species Cu, Ag, and Au. Fig. 7 shows the spin textures for the $M(111)/\alpha$ -Bi₂O₃ system. The anisotropic Rashba spin structures are shown for $M = \text{Cu}$ (Fig. 7 (b)) and for $M = \text{Ag}$ (Fig. 7 (c)), while the non-Rashba type spin structures are shown for $M = \text{Au}$ (Fig. 7 (d)). Since α -Bi₂O₃ is monoclinic (P2₁/c, No. 14) and C-point is Brillouin zone-boundary, each system has no 4-fold rotational symmetry (around C-point) that makes Fermi surface and spin textures isotropic. The anisotropic Rashba spin vortices for $M = \text{Cu}$ and Ag are opposite to each other (e.g. The vortex for lower energy bands shown in Fig. 7, $M = \text{Cu}$ is the clockwise, while that for $M = \text{Ag}$ is the anti-clockwise.), which may support experimental result [21] that the sign of α_R^{exp} in Ag(111)/Bi₂O₃ is positive while that in Cu(111)/Bi₂O₃ is negative. For $M = \text{Au}$, there are non-Rashba type spin splitting. This may be due to strong SOC of Au. On the other hand, in the experiment, a symmetric circular spin structure was observed by angle dependence results but not an anisotropic one, because the amorphous Bi₂O₃ results in a symmetric potential in x-y plane.

5 Summary

We have studied the systems with special spin structures applicable to spintronics or thermoelectric conversion based on first-principles density functional calculations using OpenMX [5]. We focused on surfaces, interfaces and 2D system with peculiar spin textures such as skyrmion crystals in real space that can enhance Berry curvatures in momentum space and anomalous Nernst effect. The Rashba spin textures in momentum space can lead to spin-to-charge conversion (from a spin current to a charge current). Recently, we also discussed photo-induced spin to charge conversion [22].

We also study other spin textures, non-collinear spin structures in real space for computational design for quantum spin ice [23] and collinear spin textures in momentum space, i.e., persistent spin helix states that can lead to long spin lifetime[24,25].

Acknowledgement

The author acknowledges the collaboration with H. Kotaka, Y.P. Mizuta, N. Yamaguchi, S. Minami, H. Sawahata, M. Sugita, Y. Tanaka, and M. Saito.

References

- [1] Y. Otani, M. Shiraishi, A. Ohiwa, E. Saito, and S. Murakami, *Nat. Phys.* **13** (2017) 829.
- [2] N. Nagaosa, J. Sinova, S. Onoda, A. H. MacDonald, and N.P. Ong, *Rev. Mod. Phys.* **82** (2010)1539.
- [3] Y. A. Bychkov, and E. I. Rashba, *J. Phys. C* **17**(1984) 6039.
- [4] B. Bernevig, J. Orenstein, and S. Zhang, *Phys. Rev. Lett.* **97** (2006) 236601.
- [5] T. Ozaki et al., Open source package for Material eXplorer, <http://www.openmx-square.org>
- [6] Y.P. Mizuta and F. Ishii, *Sci. Rep.* **6** (2016) 28076.
- [7] Y.P. Mizuta, H. Sawahata, F. Ishii, *Phys. Rev. B* **98** (2018) 205125.
- [8] U. von Barth and L. Hedin, *J. Phys. C* **5** (1972) 1629.
- [9] J. Kübler, K. H. Höck, J. Sticht, and A. R. Williams, *J. Phys. F* **18** (1988) 469.
- [10] J. P. Perdew, K. Burke, and M. Ernzerhof, *Phys. Rev. Lett.* **77** (1996) 3865.
- [11] I. Morrison, D. M. Bylander, and L. Kleinman, *Phys. Rev. B* **47** (1993) 6728.
- [12] G. Theurich and N. A. Hill, *Phys. Rev. B* **64** (2001) 073106.
- [13] T. Ozaki, *Phys. Rev. B* **67** (2003) 155108.
- [14] T. Ozaki and H. Kino, *Phys. Rev. B* **69** (2004) 195113.
- [15] A. A. Mostofi, J. R. Yates, G. Pizzi, Y.-S. Lee, I. Souza, D. Vanderbilt, and N. Marzari, *Comput. Phys. Commun.* **185** (2014) 2309.
- [16] G. Pizzi, D. Volja, B. Kozinsky, M. Fornari, and N. Marzari, *Comput. Phys. Commun.* **185** (2014) 422.
- [17] S. Minami, F. Ishii, Y.P. Mizuta, and M. Saito, *Appl. Phys. Lett.* **113** (2018) 032403.

- [18] T. Fukui, Y. Hatsugai, H. Suzuki, *J. Phys. Soc. Jpn.*, **74** (2005) 1674.
- [19] R. J. Sánchez, L. Vila, G. Desfonds, S. Gambarelli, J. Attané, D. J. Teresa, C. Magén, and A. Fert, *Nat. Commun.* **4** (2013) 2944.
- [20] V. M. Edelstein, *Solid. State. Commun.* **73** (1990) 233.
- [21] H. Tsai, S. Karube, K. Kondou, N. Yamaguchi, F. Ishii, Y. Otani, *Sci. Rep.* **8** (2018) 5564.
- [22] J. Puebla, F. Auvray, N. Yamaguchi, M. Xu, S.Z. Bisri, Y. Iwasa, F. Ishii, and Y. Otani, *Phys. Rev. Lett.* **122** (2019) 256401.
- [23] S. Onoda and F. Ishii, *Phys. Rev. Lett.* **122** (2019) 067201.
- [24] M. A. Absor, F. Ishii, H. Kotaka, and M. Saito, *App. Phys. Express* **8** (2015) 073006.
- [25] N. Yamaguchi and F. Ishii, *App. Phys. Express* **10** (2017) 123003.